

# Atomic-Scale Structure and Stress Release Mechanism in Core–Shell Nanoparticles

Michael Nathanson,<sup>†</sup> Krishan Kanhaiya,<sup>†</sup> Alan Pryor, Jr.,<sup>‡</sup> Jianwei Miao,<sup>‡</sup> and Hendrik Heinz<sup>\*,†,‡</sup>

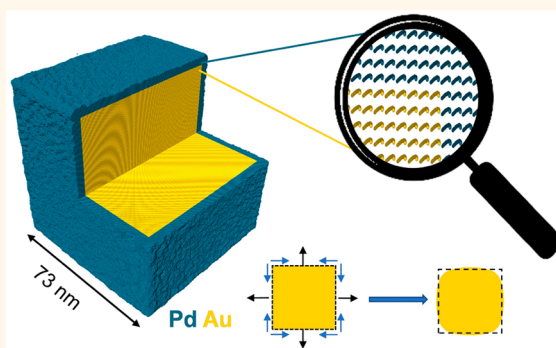
<sup>†</sup>Department of Chemical and Biological Engineering, University of Colorado at Boulder, Boulder, Colorado 80309, United States

<sup>‡</sup>Department of Physics & Astronomy and California NanoSystems Institute, University of California, Los Angeles, California 90095, United States

## S Supporting Information

**ABSTRACT:** Core–shell nanoparticles find applications in catalysts, sensors, and theranostics. The full internal 3D atomic structure, however, cannot be resolved by current imaging and diffraction techniques. We analyzed the atomic positions and stress-release mechanism in a cubic Au–Pd core–shell nanoparticle in approximately 1000 times higher resolution than current experimental techniques using large-scale molecular dynamics simulation to overcome these limitations. The core–shell nanocube of 73 nm size was modeled similarly to solution synthesis by random epitaxial deposition of a 4 nm thick shell of Pd atoms onto a Au core of 65 nm side length using reliable interatomic potentials. The internal structure reveals specific deformations and stress relaxation mechanisms that are caused by the +4.8% lattice mismatch of gold relative to palladium and differential confinement of extended particle facets, edges, and corners by one, two, or three Au–Pd interfaces, respectively. The three-dimensional lattice strain causes long-range, arc-like bending of atomic rows along the faces and edges of the particle, especially near the Au–Pd interface, a bulging deformation of the Pd shell, and stacking faults in the Pd shell at the corners of the particle. The strain pattern and mechanism of stress release were further characterized by profiles of the atomic layer spacing in the principal crystallographic directions. Accordingly, strain in the Pd shell is several times larger in the extended facets than near the edges and corners of the nanoparticle, which likely affects adsorption, optical, and electrochemical properties. The findings are consistent with available experimental data, including 3D reconstructions of the same cubic nanoparticle by coherent diffractive imaging (CDI) and may be verified by more powerful experimental techniques in the future. The stress release mechanisms are representative for cubic core–shell nanoparticles with fcc structure and can be explored for different shapes by the same methods.

**KEYWORDS:** nanoparticles, interfaces, lattice strain, molecular dynamics simulation, stress release, coherent diffractive imaging, atomic resolution



Core–shell nanoparticles find applications in catalysis, sensors, and biomedical imaging due to different properties at the interface of the two materials and the possibility to choose from a wide range of compositions.<sup>1–4</sup> The properties of core–shell nanoparticles can be finely tuned by adjusting the size, shape, and shell thickness through synthesis methods with sub-nanometer precision.<sup>2,5–8</sup> A typical feature of these nanostructures is a lattice mismatch that contributes to the observed functionality. For example, bulk Au and Pd lattices have the same fcc crystal structure although the lattice constants differ +4.8% relative to each other, known to be 4.078 and 3.891 Å, respectively.<sup>9</sup> The stress along the boundary of the two metals contributes to different characteristics of the thin shell and specific properties of core–shell nanoparticles in comparison to bulk metal.<sup>10</sup>

The boundaries of the two metals have been probed on extended (100)<sup>10–14</sup> and (111)<sup>15,16</sup> surfaces as well as on multisurface nanocrystals of few nanometer size,<sup>7,17,18</sup> primarily through use of transmission electron microscopy (TEM). Conversely, the 3D internal atomic structure of core–shell nanoparticles larger than a few nanometers remains an open question. Mechanisms for stress release were proposed that combine Shockley partial dislocations with stacking faults to allow a transition from pseudomorphic epitaxial growth to the lattice structure of the bulk metals. The transition was reported at different distances from the interface depending on

Received: August 11, 2018

Accepted: November 20, 2018

Published: November 20, 2018

**Table 1. Comparison of Metal Properties According to Experiments, Simulations with the Interface Force Field (IFF) Employed Here, and Other Simulation Methods<sup>a</sup>**

metal	method	$a$ (Å)	$\gamma_{SV}$ {111} (J/m <sup>2</sup> )	$E$ (GPa)	$K$ (GPa)	$\gamma_{USF}$ (mJ/m <sup>2</sup> )	$\gamma_{SF}$ (mJ/m <sup>2</sup> )
Pd	experiment	3.890 <sup>27</sup>	1.98 <sup>30</sup>	146 <sup>27</sup>	193 <sup>27</sup>	$b$	130–180 <sup>34,35,37c</sup>
	IFF	3.892 <sup>22</sup>	1.98 <sup>22</sup>	146 <sup>22</sup>	182 <sup>22</sup>	271	3.5
	EAM	3.890 <sup>28d</sup>	1.22 <sup>28</sup>	190 <sup>28</sup>	195 <sup>28d</sup>	162–218 <sup>13</sup>	51–85 <sup>13</sup>
	DFT	3.980 <sup>29</sup>	1.31–1.87 <sup>29</sup>	99 <sup>31</sup>	163, <sup>29</sup> 186 <sup>31</sup>	265 <sup>33</sup>	186 <sup>33</sup>
Au	experiment	4.078 <sup>27</sup>	1.54 <sup>30</sup>	88 <sup>27</sup>	173 <sup>27</sup>	$b$	30–32 <sup>36,37c</sup>
	IFF	4.078 <sup>22</sup>	1.54 <sup>22</sup>	110 <sup>22</sup>	133 <sup>22</sup>	199	2
	EAM	4.090 <sup>28d</sup>	0.79 <sup>28</sup>	132 <sup>28</sup>	167 <sup>28d</sup>	110 <sup>28</sup>	5 <sup>28</sup>
	DFT	4.160 <sup>29</sup>	0.74–1.04 <sup>29</sup>	59, <sup>32</sup> 73 <sup>31</sup>	140, <sup>29</sup> 192, <sup>32</sup> 164 <sup>31</sup>	134 <sup>37c</sup>	33 <sup>37c</sup>

<sup>a</sup>Properties include the fcc lattice constant ( $a$ ), the {111} surface energy ( $\gamma_{SV}$ ), Young's modulus ( $E$ ), bulk modulus ( $K$ ), the activation energy to form stacking faults (unstable stacking fault energy) ( $\gamma_{USF}$ ), and the equilibrium stacking fault energy ( $\gamma_{SF}$ ). <sup>b</sup>Not available. <sup>c</sup>Uncertainties are associated with rolling, node radii, and other defects. <sup>d</sup>The value was fixed during parametrization.

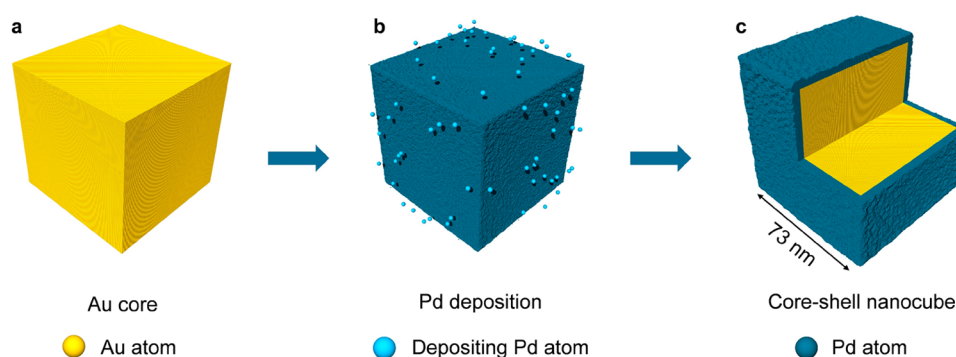


**Figure 1. Generation of a model of a core-shell Au-Pd nanoparticle by random isotropic epitaxial atom deposition in the simulation. (a) The initial Au core. (b) Evolution of the particle structure as Pd atoms are deposited. Depositing atoms are shown as larger spheres in light blue color. (c) The complete core-shell particle. The open section visualizes core and shell.**

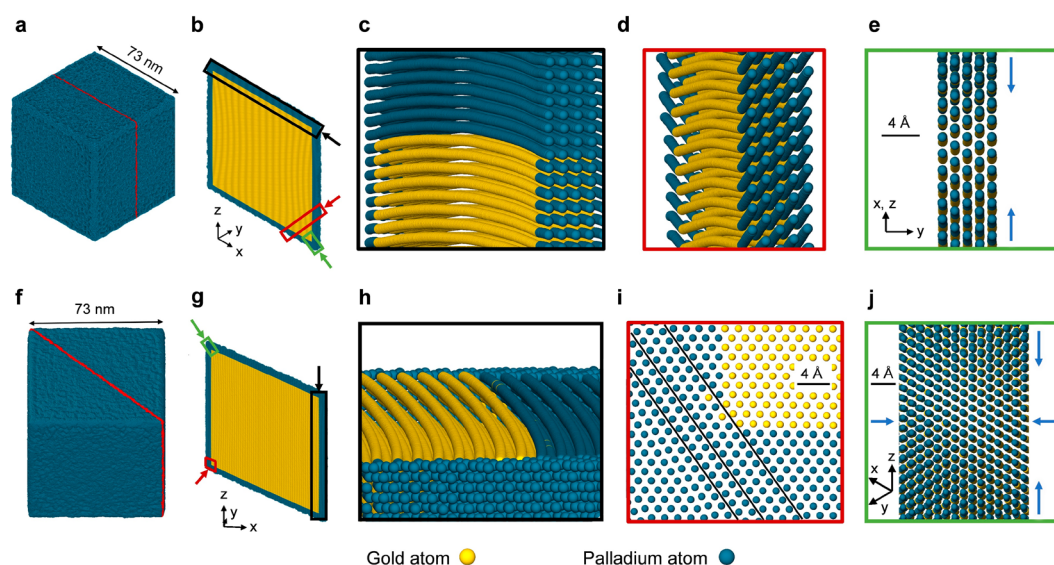


**Figure 2. Visualization of internal atomic displacements and associated strain in the epitaxially grown Au-Pd core-shell nanoparticle from molecular dynamics simulation. (a) A (100) slice through the model particle, indicated by the red line. (b) Atomic structure of the (100) slice and projections for panels c–e: (c) Along the flat surfaces, long-range arcs can be seen that have an amplitude of about 2 Å. (d) Across edges, indents in Au due to compressive strain from two Pd boundaries are observed. (e) Pd atoms are compressed near the edges to transition from an expanded epitaxial lattice toward the equilibrium lattice of bulk Pd (blue arrows). (f) A (110) slice through the model particle, indicated by the red line. (g) Atomic structure of the (110) slice and projections for panels h–j): (h) Along the edges, long-range arcs with an amplitude of about 2 Å are seen similar to those on the flat surfaces. (i) At the corners, stacking faults occur along the (111) plane, highlighted by solid lines. (j) The top view onto the corner shows compression of Pd atoms from an expanded epitaxial lattice toward the equilibrium Pd lattice both parallel and perpendicular to the slice (blue arrows).**

the ( $hkl$ ) facet. Thereby, formation of stacking faults is only possible along (111) planes. The development of a bulk Pd

lattice atop a Au(111) surface has been reported as close as eight atomic layers from the interface,<sup>14</sup> and a gradual lattice

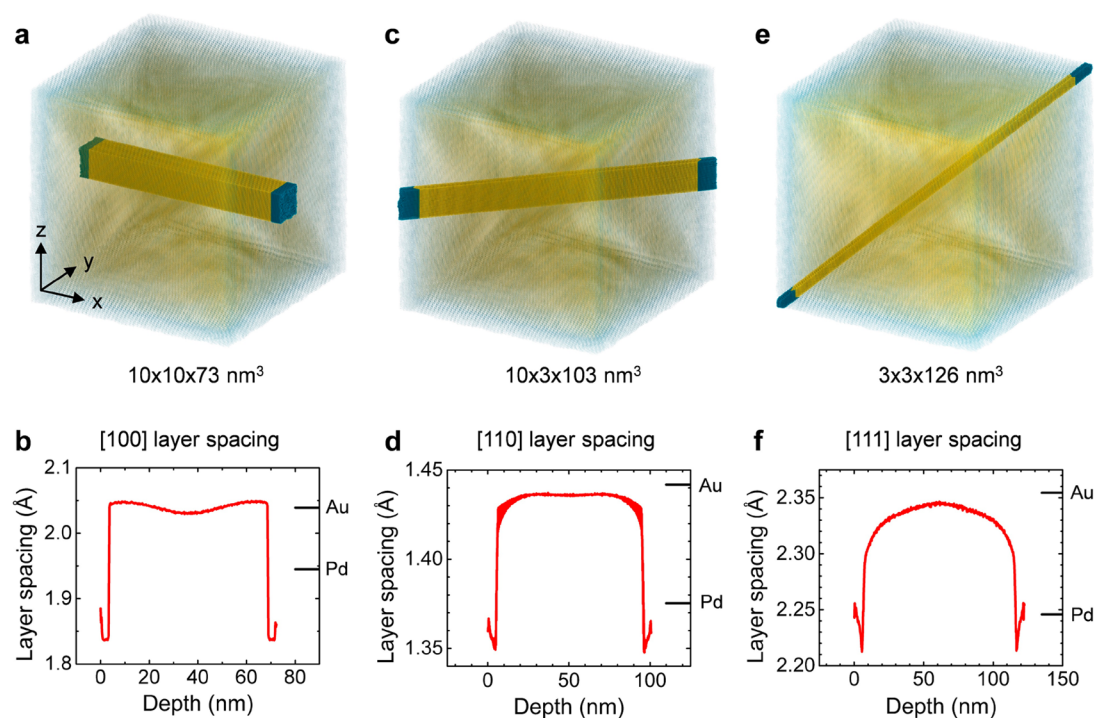


**Figure 3.** Profiles of the atomic layer spacing in the principal crystallographic directions. The layer spacing of ideal Au and Pd lattices is indicated for comparison. (a, b) Profile for a slab cut vertical to the flat Au–Pd interfaces in the [100] direction. (c, d) Profile for a slab cut vertical to the edges in the [110] direction. (e, f) Profile for a slab cut vertical through the corners in the [111] direction.

transition of Pd atop a Au(100) surface has been reported between 6 and 30 atomic layers.<sup>12</sup> Observations of alloying to relieve stress along the boundary are also known; however, annealing of the particle well above room temperature was necessary.<sup>17,19</sup> Molecular dynamics (MD) studies using embedded atom method (EAM) potentials have suggested that Pd deposited on Au(100) surfaces produces stacking faults along (111) planes after 9 atomic layers of deposition, allowing the Pd to relax to its normal lattice.<sup>13</sup>

The internal structure of larger core–shell nanoparticles remains uncertain. Coherent diffraction imaging (CDI) reaches nanometer resolution and cannot currently probe the atomic-level structure.<sup>20</sup> To overcome these limitations, we carried out large-scale molecular dynamics simulations that achieve picometer resolution and observed deformations at the boundary of the two metals. The chosen system was a Au–Pd core–shell nanoparticle containing 23 million atoms, grown with epitaxial interfaces as expected in solution synthesis and by vapor deposition, as well as with hypothetical hetero-epitaxial interfaces (see [Supporting Information](#)). The molecular dynamics simulations utilized the Interface Force Field (IFF), which accurately reproduces the metal lattice structures, surface, and interfacial energies (Table 1).<sup>21,22</sup> We explain the characteristic deformation patterns at the Au–Pd interface in the context of the strain field and available experimental data,<sup>20,23–25</sup> as well as insights from previous simulations. Prior simulations have been limited to flat surfaces of about 100 000 atoms<sup>13</sup> or nanoparticles of less than 5000 atoms<sup>19,26</sup> and oftentimes used more approximate potentials.

## RESULTS AND DISCUSSION

**Epitaxial Deposition Model.** The epitaxial atomic deposition model represents the structure of core–shell nanoparticles grown in solution, by atomic layer deposition,

or by chemical vapor deposition (Figure 1). Model building involved the simulation of Pd atom deposition onto the Au core and resulted in epitaxial growth for the entire 4 nm thick shell of 20 atomic layers (Figure 2). Details of the model building, the potentials, and the simulation methods are described in the [Methods](#) section. The observation of epitaxial growth in the model is consistent with experimental data for flat surfaces, which suggest epitaxial growth for at least the first 6 to 13 atomic layers in the outer shell,<sup>12</sup> and with previous molecular dynamics simulations that suggest epitaxial growth for 8 or more atomic layers in the outer shell.<sup>13</sup> As a difference to extended surfaces, three-dimensional nanoparticles have also been suggested to sustain significantly more strain, shifting the critical layer of the transition from epitaxial growth to the bulk lattice spacing further away from the metal–metal interface,<sup>18</sup> which concurs with our observations of 20 epitaxial atomic layers.

**Atomic-Level Strain.** The atomic-level strain in the Au–Pd nanoparticle is visualized from different perspectives (Figure 2). A (100) slice in the particle (Figure 2a,b) shows a perspective along the face of the particle (Figure 2c), across an edge (Figure 2d), and onto an edge (Figure 2e). A (110) slice in the particle (Figure 2f,g) displays a view along an edge (Figure 2h), across a corner (Figure 2i), and onto a corner (Figure 2j). We observed the formation of long-range arcs along the Au–Pd interfaces, including toward the edges (Figure 2c,h). At the center of each bounding (100) facet, the atoms are approximately 2 Å displaced relative to the atoms in the same row near the edges. The arcs proceed along the entire interface (65 nm) and all the way to the edges. Across the edges, the Au atoms are inwardly compressed toward the center of the particle (Figure 2d). Near the corners, stacking faults that form on the (111) plane extending from the corner toward the Au–Pd interface (Figure 2i) are visible.

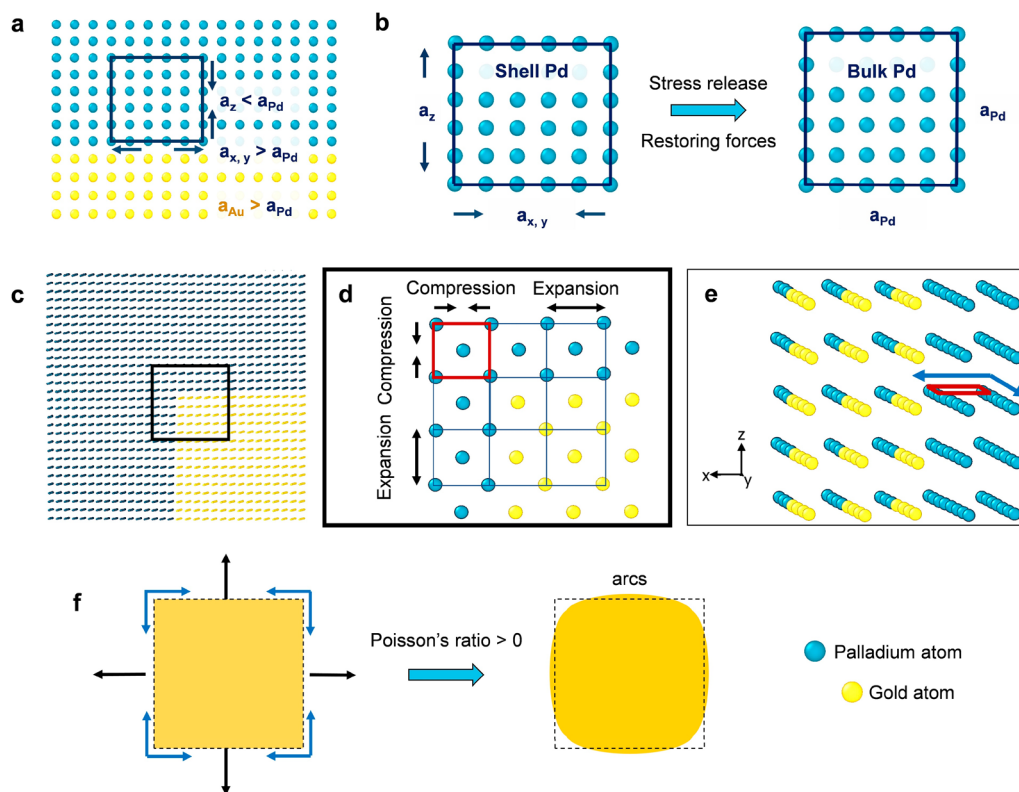


**Figure 4.** Stress release mechanism in the core–shell nanoparticle. (a) The Pd lattice with equilibrium lattice constant  $a_{Pd}$  expands to that of Au ( $a_{Au}$ ) parallel to the interface ( $a_x$  and  $a_y$ ) and contracts vertical to the interface ( $a_z$ ) to maintain the equilibrium Pd density. (b) The restoring forces in the Pd lattice attempt to relax the Pd lattice into equilibrium dimensions and superimpose along the edges of the Au–Pd interface. (c) Distorted Pd lattices meet and superimpose along the edges of the Au–Pd interface. (d) A locally denser Pd lattice emerges near the edges (red square) compared to the center of flat interfaces as a result of compression along two facets. (e) The denser Pd lattice exerts stronger compressive forces on the Au lattice and compresses the edges of the gold core (blue arrows). (f) The restoring forces combine across particle edges and lead to displacements perpendicular to the interfaces (black arrows), resulting in a bulging deformation including arc-like atomic rows. The resulting expansion is exaggerated to aid in visualization.

Compression of the Pd rows toward the edges (Figure 2e) and corners (Figure 2j) is observed. Multiple distorted Pd lattices meet at these locations, and the lattice spacing tends to shift from the equilibrium Au lattice spacing to the equilibrium Pd lattice over a shorter distance from the Au–Pd interface compared to the flat interfaces in the center of the (100) facets (Figure 2c). The arc-like bending of rows of atoms and the stacking faults are the only notable defects. Stacking faults are only observed at the corners (Figure 2i) and not seen along (100) surfaces. Prior experiments on much smaller Au–Pd core–shell nanoparticles consistently identified stacking faults preferentially outside the (111) surface of more complex Au cores in the first 3 to 6 layers of Pd to support the release of strain caused by the lattice mismatch, which agrees with the observations here (Figure 2i).<sup>18</sup> On higher index planes of core–shell nanoparticles, no lattice disruption was seen in HRTEM images, indicating heteroepitaxial growth.<sup>8</sup> Stacking faults also emerged upon Pd growth on flat periodic Au(100) surfaces in a grid-like pattern along (111) planes after about 9 atomic layers in prior MD simulations,<sup>13</sup> allowing for the relaxation of the Pd lattice on the flat Au slab. The results here indicate that the three-dimensional structure of the cubic core–shell nanoparticle allows for an alternate stress release mechanism before stacking faults would form along the (100) faces of the particle, supported by previous experimental work.<sup>18</sup> As the epitaxial growth continues into more layers, it is

likely that a network of stacking faults would form in order to allow partial edge dislocations. The dislocations would then insert additional Pd rows further from the Au–Pd interfaces to match the lattice parameter in the Pd shell to that of bulk Pd.

**Atomic Layer Spacing.** The 3D distortions throughout the particle were further characterized by profiles of the atomic layer spacing (Figure 3). One profile in the [100] direction was recorded through the center of the particle as an average over a  $10 \times 10 \text{ nm}^2$  slab (Figure 3a,b). Profiles were also computed along the planar diagonal in the [110] direction (Figure 3c,d) and along the space diagonal in the [111] direction (Figure 3e,f). The latter two profiles are over 100 nm long and utilize thinner slabs. The  $[hkl]$  profiles reveal the internal strain in the lattice compared to equilibrium fcc lattices of bulk Au and bulk Pd (Figure 3b,d,f), which is shown here in high resolution. The [100] atomic layer spacing shows that the Pd lattice is compressed perpendicular to the Au–Pd interface ( $x$  direction at 4 and 69 nm) from  $\sim 1.95 \text{ \AA}$  to  $\sim 1.83 \text{ \AA}$  (Figure 3b). The compression occurs because the other two directions ( $y$  and  $z$ ) of the Pd lattice expand to match the 4.8% wider spacing of the Au lattice. This significant distortion of the outer Pd shell is likely to affect the interaction with adsorbed molecules, including surface reactivity and electrocatalytic properties. Compression of the Pd layer spacing is slightly relieved at the outer boundary (0 and 73 nm) due to the surface roughness of the particle (Figure 1c). The Au layer spacing near the Au–Pd

interface slightly expands perpendicular to the interface plane (in the  $x$  direction at 4–23 nm and 50–69 nm) in response to some compression by the epitaxial Pd lattice in the other directions ( $y$  and  $z$ ) (Figure 3b). This mismatch contributes to the arc-like features (Figure 2c,h). Toward the center of the particle, the Au lattice relaxes toward the normal lattice spacing and is even compressed to a small extent (23–50 nm). The small overall net compression of Au is a result of the confining outer Pd lattice, and the amplitude of the arc-like features decreases further inside the particle. At a distance of 15 nm from the Au–Pd interface into the gold core, the amplitude of the arcs is reduced to 20% of the maximum amplitude.

Compression of the Pd atomic layer spacing is also seen in the [110] direction through the edges of the nanoparticle (Figure 3c,d). The maximum compression of Pd atomic layers normal to the Au–Pd interface at 5–6 nm and at 97–98 nm is less significant compared to the flat interfaces (1.8% instead of 6.2%), and the layer spacing continually expands toward the outside of the particle (Figure 3d). The compression in the [110] direction near the Au–Pd interface compensates the epitaxial expansion of the Pd lattice to the Au lattice spacing in the (110) plane perpendicular to the [110] direction, and the following partial expansion in the [110] direction toward the normal Pd lattice spacing (0–5 and 98–103 nm) is coupled with the partial compression of Pd atomic rows perpendicular to the [110] direction (Figure 2e). Therefore, the nanoparticle edges show more relaxation of the Pd lattice toward Pd bulk properties than the extended facets, and the Pd lattice strain is much reduced near the edges. The Pd lattice near the edges also encloses the inner Au lattice on two sides, the (100) and (010) planes, which leads to a consistent small net compression of the Au atomic layer spacing in the [110] direction of  $\sim 0.3\%$ , especially near the edges (7–25 and 78–96 nm) where the contraction can exceed 1% (Figure 3d). The compression of the Au layer spacing in the [110] direction bounded by two blocks of Pd (Figure 3c,d) is in contrast to the expansion in the [100] direction bounded by only one block of Pd at the flat Au–Pd interface (Figure 3a,b).

The [111] direction profile shows similar but more extreme trends compared to the [110] profile (Figure 3f). The Pd layer spacing at the interface is contracted and normal Pd layer spacing is reached toward the outside corners due to the presence of stacking faults (Figure 2i). The Pd surface near the corners of the nanoparticle is therefore virtually free of strain and stress. The inner Au lattice near the nanoparticle corners interacts with three Pd lattice interfaces, which leads to significant compression of the Au lattice in excess of 2% (Figure 3f). The distortion of the Au lattice is more extreme and penetrates further into the Au lattice than at the edges (Figure 3d). The trend toward contraction of the Au lattice at the corners and edges versus expansion vertical to the (100) Au–Pd interfaces causes the observed arc-like deformations (Figure 2c,d,h). Details of the calculations of layer spacing profiles can be found in Section S2 in the Supporting Information.

**Stress Release Mechanism.** The epitaxial growth of Pd on the Au lattice produces strain in both lattices (Figure 4). The deposited Pd lattice expands in the  $x$  and  $y$  directions parallel to the Au–Pd interface and experiences compression in the  $z$  direction relative to bulk Pd (blue arrows in Figure 4a). The strain in the Pd lattice creates restoring forces in the opposite directions (blue arrows in Figure 4b), and the atoms in the distorted Pd lattice of the shell attempt to relax into the

bulk Pd lattice. At the edges, the effect is particularly strong as two distorted Pd lattices meet and create compression along two facets (Figure 4c,d). Expansion remains possible only in one direction (vertical to the red square). The in-plane compression results in an overall density increase in Pd at the edges and in stronger interfacial forces than on the facets of the particle (Figure 4e). The incommensurate lattice of the gold core at the edges is therefore forced more strongly into compliance with the Pd shell than on the facets of the particle. This effect is even increased in corners where Pd compression occurs on all three facets and enforces a significant reduction in the Au(111) atomic layer spacing (Figure 3f). The restoring forces on Au act toward the center of the faces (blue arrows in Figure 4e,f) and create the strain patterns observed throughout the particle including the arc-like bending of atomic rows (Figure 2). The particle expands out from the center of the facets (black arrows in Figure 4f) because the Poisson ratio  $\nu$  of each metal is greater than zero and it would require more energy to compress the entire particle than to allow expansion in this bulging fashion when a force parallel to the Au–Pd interfaces is applied from both sides ( $\nu = 0.5 - E/6B$  with  $B > E$  in Table 1). The stress spreads across many atoms in the large particle and creates strain in three dimensions, and the model particle does not overcome the energy barrier to create stacking faults and partial dislocations along the faces in the Pd shell with approximately 20 deposited atomic layers. Prior studies suggest that such defects would be observed closer to the Au–Pd interface on flat substrates.<sup>12,13</sup> On the nanoparticle, we observed stacking faults at the corners where three facets, three edges, and their strain fields meet (Figure 2i).

**Comparison with Coherent Diffraction Imaging.** The structure of the model nanoparticle is in excellent agreement with the structure of a nanoparticle that has the same composition and size and was analyzed by X-ray coherent diffractive imaging (CDI) (Figure 5).<sup>20</sup> The direct comparison between experimentally measured CDI patterns (Figure 5a,b) and computed CDI patterns from the atomistic models (Figure 5c,d) shows highly similar patterns that differ mainly in resolution. The experimentally acquired diffraction patterns utilized an X-ray free electron laser (XFEL) (Figure 5a,b),<sup>20</sup> and the simulated diffraction patterns were obtained from the atomistic model in equilibrium, matching the simulation conditions to the experiment with  $5.0 \times 10^{11}$  photons per pulse focused to a  $1.5 \mu\text{m}$  spot size (Figure 5c,d). The resolution of the diffraction patterns is currently limited to 6.1 nm in experiment and in the range of 0.1 to 1 pm in molecular dynamics simulation. Accordingly, the definition of the CDI patterns from molecular dynamics simulation appears higher (Figure 5c,d). The results are in close agreement ( $R$ -factor = 0.18), especially given that the experimental data provide incomplete information for the model, such as an approximate total number count of atoms and their expected positions and no resolution of the internal structure of the nanoparticle. The analysis by molecular dynamics simulations using additional hypotheses about the internal structure, such as the likely epitaxial deposition model and a hypothetical heteroepitaxial model (see Supporting Information), therefore provides insights in higher resolution than current experimental methods for nanoparticles of this size, and the predictions can be verified as experimental methods advance.

CDI is a quantitative imaging technique capable of measuring the electron density of samples at high-resolution in 3D without the requirement of lenses.<sup>38–40</sup> Using a coherent

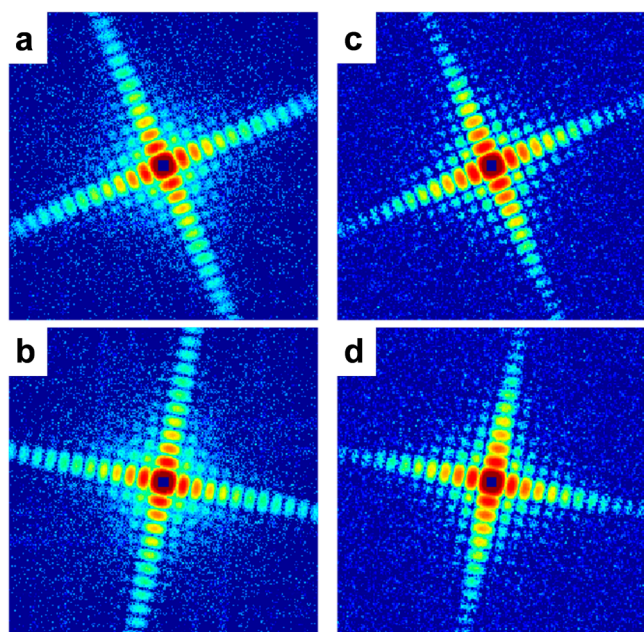


**Figure 5.** Coherent diffractive imaging (CDI) patterns of Au–Pd core–shell nanoparticles in experiment and computed from the model. (a, b) Experimental CDI patterns measured from a Au–Pd core–shell nanoparticle at two different orientations (resolution 6.1 nm).<sup>20</sup> (c, d) Corresponding CDI patterns computed from the epitaxial nanoparticle model at two different orientations using the same algorithm. Poisson noise was added to the simulated diffraction patterns, and the definition appears higher than in experiment. The model provides details in all-atom resolution and matches the experiment with an *R*-factor of 0.18.

X-ray source, far-field diffraction patterns of a noncrystalline sample or a nanocrystal can be measured and subsequently converted to real-space reconstructions by application of an iterative phase retrieval algorithm.<sup>41</sup> The hypothetical limit of the diffraction-limited resolution in CDI is only a few angstroms but hindered here by the achievable signal-to-noise ratio of the diffraction data. Current experimental practice allows a resolution of 5–6 nm for the large system and a resolution of 1–2 nm in smaller systems.<sup>20,40</sup> The advent of the X-ray free electron laser (XFEL) offers an opportunity to close the gap to the theoretical limit (angstroms) by providing extraordinary X-ray brilliance and, therefore, high signal in a single pulse. However, the sample is destroyed after one exposure, and acquisition of a tilt series necessary for full 3D reconstruction using traditional tomographic techniques is not feasible.<sup>42</sup> Recent work demonstrates that for symmetric nanoparticles, exploitation of symmetry operations along with consideration of Ewald sphere curvature can facilitate 3D reconstructions of nanoparticles from single diffraction patterns,<sup>20,43,44</sup> and further developments may reach 3D reconstructions in angstrom resolution.<sup>38–40</sup>

In addition to advances in CDI, atomic electron tomography (AET) has been developed to image the 3D atomic structure of crystal defects such as grain boundaries and edge and screw dislocations, as well as stacking faults.<sup>25,45,46</sup> AET has been applied to determine the 3D coordinates of individual atoms in materials with high precision, allowing the direct measurement of the strain tensor and the observation of chemical order/disorder, point defects, and nucleation dynamics.<sup>23,24,47</sup> Even though the current limit is tens of thousands of atoms, we

expect to use AET to experimentally verify the arc-like atomic deformations and strain reported in this work. Measured 3D atomic coordinates by AET can be used as direct input for molecular dynamics and density functional theory simulations to correlate 3D structures with material properties at the single-atom level.<sup>23,47</sup>

**Applicability to Other Core–Shell Nanoparticles.** The proposed stress release mechanism applies to cubic-shaped fcc nanoparticles of different composition and size, and additional considerations would be necessary for other shapes. For cube-shaped fcc nanoparticles, the lattice mismatch, the particle size, and the activation energy to form stacking faults determine the magnitude of internal deformations and stress. Qualitatively similar strain patterns are expected when the composition or size changes because differences in confinement at extended facets (one interface), edges (two interfaces), and corners (three interfaces) will similarly occur (Figure 4). The magnitude of internal deformations is expected to scale with the difference in lattice parameters between the two metals, whereby a lattice mismatch in excess of 5% could lead to heteroepitaxial deposition (see Figures S1 to S4 and Section S1 in the Supporting Information).<sup>7</sup> For example, Au–Pd particles grow epitaxially, while Ag–Pd particles with a larger lattice mismatch grow heteroepitaxially. The minimum particle size to observe notable deformations is about 10 nm, which is necessary to develop sufficient differences in confinement on facets, edges, and corners that lead to the patterns reported. The 73 nm epitaxial particle shows arc-like deformations of 0.2 nm amplitude. The corresponding heteroepitaxial particle shows spiral-like deformations of 0.1 nm amplitude as well as gaps of one row of atoms every  $\sim 10$  nm (see Figure S2 in the Supporting Information), indicating the critical particle size to develop significant strain patterns. In addition, the extent of formation of stacking faults near the corners will scale with the activation energy  $\gamma_{\text{USF}}$  to form stacking faults (Table 1). At a critical number of atomic layers of the shell, stacking faults along with Shockley partial dislocations are expected to develop along (111) planes on top of (100) facets to release stress.<sup>13</sup>

The stress relaxation mechanism for core–shell nanoparticles bounded by (111) facets, rather than (100) facets, differs from the mechanism reported here. Shockley partial dislocations and stacking faults would form on (111) facets,<sup>18</sup> which is geometrically not feasible parallel to (100) facets. Core–shell nanoparticles with shapes that are bounded by multiple different (*hkl*) facets would likely exhibit grain boundaries and a superposition of stacking faults on (111) facets, as well as epitaxial/heteroepitaxial relaxation mechanisms on (100) facets. The atom deposition rate and thickness of the shell could also become nonuniform on different (*hkl*) bounding facets and depend on the reaction conditions.<sup>7,8</sup>

In addition, the stress relaxation mechanism can be influenced by co-deposition of atoms, interdiffusion, truncation of edges, atomic defects, and steps along the interface. In case of cubic-shaped fcc core–shell nanoparticles, such effects would superimpose local stresses and deformations while the global stress relaxation mechanism remains the same as described.

## CONCLUSIONS

We employed all-atom classical molecular dynamics simulation to model the growth of Au–Pd core–shell nanocubes of 73 nm size and obtained insights into the internal structure in a

resolution approximately 3 orders of magnitude higher than current experiments. On Au(100) facets, an epitaxial growth mechanism of Pd was observed for at least 4 nm in shell thickness. The lattice mismatch of +4.8% of Au versus Pd causes arc-like deformations of atomic rows across the entire Au–Pd interface, spatially variable atomic layer spacing, and the formation of stacking faults inside the Pd corners. The largest lattice strain on the outer Pd surface of the nanoparticle is found on the extended facets, followed by significantly lower strain near the edges, and virtually stress-free corners. The cause for the strain patterns is the confinement of the inner Au core by the overgrown Pd lattice that exerts significantly more stress at the corners and at the edges of the Au–Pd interface in comparison to the flat bounding facets. As a result, the nanoparticle tends to expand at the center of the facets in a bulging deformation and aligns more closely with the equilibrium Pd lattice structure near the edges and the corners. The amount of lattice mismatch and the particle size determine the extent of the reported internal deformations, and the findings can be applied to cubic core–shell nanoparticles with fcc structure of other compositions and sizes.

The ability to produce stable and significantly strained metal facets on core–shell nanoparticles may be exploited to tune selective adsorption, surface reactivity, and electrocatalytic properties. Internal distortions also influence optical properties, which may be utilized in sensors, catalysts, and electrode materials. Finally, the study shows that simulation methods can be employed to predict the likely three-dimensional atomic positions of large nanostructures in high resolution and guide in the rational design of materials properties alongside experiments.

## METHODS

**Model Building.** A random epitaxial deposition model of the Au–Pd core–shell nanoparticle was constructed by starting with a  $65 \times 65 \times 65 \text{ nm}^3$  Au core made of 160 repeat units of an FCC unit cell in each direction (Figure 1). The cubic Au core was placed into an  $85 \times 85 \times 85 \text{ nm}^3$  periodic box and subjected to random deposition of Pd atoms onto each facet at a rate of 1 atom per time step per facet at 298 K. The fix deposit command in LAMMPS was used for the random deposition and resulted in epitaxial deposition of Pd atoms.<sup>48</sup> In total, 6.4 million Pd atoms were deposited on top of the particle core of 16.4 million Au atoms, resulting in a total count of 22.8 million atoms in the core–shell particle model. The Pd shell was deposited in approximately 3 ns of simulation time using a time step of 2.5 fs. In addition to this random epitaxial deposition model, an alternative heteroepitaxial model of the Au–Pd nanoparticle was prepared and analyzed by placing entire Pd slabs of 4 nm thickness directly onto the Au core (Figure S1 in the Supporting Information). The visualization and analysis of this alternative heteroepitaxial model are presented in the Supporting Information (Figures S1–S4 and Section S1).

We emphasize that the models are idealized compared to experiment and illustrate the overall internal structure in the absence of common defects. For example, the random epitaxial model shows marginal mixing of Au and Pd atoms at the interface (Figure 2i) and does not consider truncation at the corners and edges of the Au core. The model also neglects atomic defects and steps at the Au–Pd interface that are likely found in experiment. Mixing of Au and Pd atoms at the interface may be significant as a result of co-deposition of both atoms during surface redox equilibria and may help reduce the local stress relative to a sharp Au–Pd interface. At the same time, atomic defects and steps at the Au–Pd interface, as well as truncation at the corners and edges of the Au core, can have many possible representations and were excluded for simplicity. The main aim of the idealized model with sharp epitaxial interfaces is to quantify the effect

of interfaces on the internal strain, while customized models with added defects can be explored in follow-on studies. A similar principal stress release mechanism is expected in the ideal model and in defective models as large portions of the bulk and interfaces remain the same so that changes in strain and stress at the interface due to local defects likely add as a superposition to the overall strain pattern.

**Simulation Details.** All simulations were performed using the LAMMPS<sup>48</sup> program, and the atomic visualizations were created using the OVITO program.<sup>49</sup> After deposition of the Pd shell, the complete model of the Au–Pd core–shell nanoparticle was allowed to reach equilibrium in the NVT ensemble in vacuum at 298 K for 1 ns with a time step of 2.5 fs. The analysis of the equilibrium crystal structure was carried out using an average structure generated from 40 frames taken over the last 200 ps of the simulation, which eliminates thermal noise and allows for the identification of equilibrium positions of the atoms, the local equilibrium lattice spacing, and long-range deformations. The calculation of the profiles of the atomic layer spacing is described in the Supporting Information (Figure S5 and Section S2).

All simulations were carried out using the Interface Force Field (IFF), which reproduces the bulk lattice parameters of Au and Pd with <0.1% deviation from experiment,<sup>22,50</sup> surface energies with <2% deviation from experiment,<sup>22,30</sup> and adsorption properties in excellent agreement with experiment and with quantum-mechanical data for small systems (Table 1).<sup>51–53</sup> Predictions of crystal growth and reaction rates in surface catalysis have also been demonstrated.<sup>54–57</sup>

Specifically, accurate surface properties are helpful to characterize the interfacial region of the core–shell nanoparticles. Mechanical properties with IFF also agree well with experiment, including deviations <5% and ~20% for the elastic moduli of Pd and Au, respectively, which is similar to Density Functional Theory (Table 1). Some deviation for the elastic moduli of Au is a limitation of the Lennard-Jones potential used in IFF<sup>21,22</sup> and related to the Poisson ratio of gold (0.41) in comparison to palladium (0.37) that slightly deviates from the ideal Poisson ratio in LJ potentials (0.37).

The potentials were also compared to determine the energy barrier  $\gamma_{\text{USF}}$  (unstable stacking fault energy) required to create a stacking fault on an ideal (111) slab of Pd since stacking faults were identified as primary defects in previous studies of smaller systems. Data from IFF, EAM, and DFT show that the barrier to form a stacking fault parallel to the (111) plane,  $\gamma_{\text{USF}}$ , scales linearly with the (111) surface energy (Table 1), and  $\gamma_{\text{USF}}$  is most consistently represented by IFF for Pd and Au (Table 1). Prior experiments indicated that the formation of stacking faults is a kinetic process<sup>55</sup> and controlled by the higher energy barrier to form stacking faults,  $\gamma_{\text{USF}}$ , rather than by the lower equilibrium energy,  $\gamma_{\text{SF}}$  (Table 1). The observation of only a few stacking faults at the corners of the Pd shell in the simulation supports this view, in spite of rather low values of  $\gamma_{\text{SF}}$ .

The thermodynamic stability of stacking faults,  $\gamma_{\text{SF}}$ , corresponds to the energy difference between a defective crystal containing a stacking fault in the (111) plane and a perfect crystal (Figure S6 and Section S3 in the Supporting Information). The values for  $\gamma_{\text{SF}}$  do not agree among IFF, EAM,<sup>13,26,28,58</sup> DFT, and experimental data (Table 1).<sup>34–37</sup> Experimental values are subject to some uncertainty by rolling, node radii, and other defects that can interfere with measurements;<sup>34</sup> however, these deviations are less than an order of magnitude. The proximity of experimental data and quantum mechanical calculations (Table 1)<sup>33,37,58,59</sup> suggests an important role of the electronic structure of the metal for  $\gamma_{\text{SF}}$ .<sup>37</sup> The origin has not been well explained to-date, and computed values using IFF and EAM potentials are too low.

In summary, IFF shows overall best agreement with experimental data, including a weakness in equilibrium stacking fault energies,  $\gamma_{\text{SF}}$ , which however does not affect crystal growth. DFT has weaknesses in surface energies,  $\gamma_{\text{SV}}$ , and unstable stacking fault energies,  $\gamma_{\text{USF}}$ , and cannot be applied to systems with millions of atoms. EAM potentials show multiple deviations from experiment. Future improvements of IFF to overcome remaining limitations may include polarizable LJ potentials<sup>53</sup> and electronically refined LJ potentials as previously shown for W.<sup>23</sup>

## ASSOCIATED CONTENT

**S** Supporting Information

The Supporting Information is available free of charge on the ACS Publications website at DOI: 10.1021/acsnano.8b06118.

Supporting figures and additional discussion of an alternative heteroepitaxial model, of the calculation of profiles of the atomic layer spacing, and of energies of generalized planar faults (PDF)

Three-dimensional representation of the epitaxial core-shell nanoparticle and internal deformations (AVI)

## AUTHOR INFORMATION

## Corresponding Author

\*hendrik.heinz@colorado.edu

## ORCID

Hendrik Heinz: 0000-0002-6776-7404

## Notes

The authors declare no competing financial interest.

## ACKNOWLEDGMENTS

This work was supported by the Office of Naval Research (ONR-MURI-N00014-14-1-0675 and N00014-16-1-2280), the National Science Foundation (DMREF 1623947 and CBET 1530790), STROBE: A National Science Foundation Science & Technology Center (DMR 1548924), the Department of Energy (DE-SC0010378), and the University of Colorado at Boulder. We acknowledge the allocation of computational resources at the Oak Ridge Leadership Computing Facility at the Oak Ridge National Laboratory, which is supported by the Office of Science of the U.S. Department of Energy under Contract No. DE-AC05-00OR22725, at the Argonne Leadership Computing Facility, which is a DOE Office of Science User Facility supported under Contract DE-AC02-06CH11357, and at the Summit supercomputer, which is supported by the National Science Foundation (award number CNS-0821794). The CDI experiment was performed at the SPring-8 Angstrom Compact Free Electron Laser in Japan (Proposal No. 2013B8014).

## REFERENCES

- (1) Henning, A. M.; Watt, J.; Miedziak, P. J.; Cheong, S.; Santonastaso, M.; Song, M.; Takeda, Y.; Kirkland, A. I.; Taylor, S. H.; Tilley, R. D. Gold-Palladium Core-Shell Nanocrystals with Size and Shape Control Optimized for Catalytic Performance. *Angew. Chem.* **2013**, *125*, 1517–1520.
- (2) Mizukoshi, Y.; Fujimoto, T.; Nagata, Y.; Oshima, R.; Maeda, Y. Characterization and Catalytic Activity of Core-Shell Structured Gold/Palladium Bimetallic Nanoparticles Synthesized by the Sonochemical Method. *J. Phys. Chem. B* **2000**, *104*, 6028–6032.
- (3) Dabbousi, B. O.; Rodriguez-Viejo, J.; Mikulec, F. V.; Heine, J. R.; Mattoussi, H.; Ober, R.; Jensen, K. F.; Bawendi, M. G. (CdSe)ZnS Core-Shell Quantum Dots: Synthesis and Characterization of a Size Series of Highly Luminescent Nanocrystallites. *J. Phys. Chem. B* **1997**, *101*, 9463–9475.
- (4) Ghosh Chaudhuri, R.; Paria, S. Core/Shell Nanoparticles: Classes, Properties, Synthesis Mechanisms, Characterization, and Applications. *Chem. Rev.* **2012**, *112*, 2373–2433.
- (5) Lu, C.-L.; Prasad, K. S.; Wu, H.-L.; Ho, J.-a. A.; Huang, M. H. Au Nanocube-Directed Fabrication of Au-Pd Core-Shell Nanocrystals with Tetrahedral, Concave Octahedral, and Octahedral Structures and Their Electrocatalytic Activity. *J. Am. Chem. Soc.* **2010**, *132*, 14546–14553.
- (6) Ferrer, D.; Torres-Castro, A.; Gao, X.; Sepúlveda-Guzmán, S.; Ortiz-Méndez, U.; José-Yacamán, M. Three-Layer Core/Shell Structure in Au-Pd Bimetallic Nanoparticles. *Nano Lett.* **2007**, *7*, 1701–1705.
- (7) Fan, F.-R.; Liu, D.-Y.; Wu, Y.-F.; Duan, S.; Xie, Z.-X.; Jiang, Z.-Y.; Tian, Z.-Q. Epitaxial Growth of Heterogeneous Metal Nanocrystals: From Gold Nano-Octahedra to Palladium and Silver Nanocubes. *J. Am. Chem. Soc.* **2008**, *130*, 6949–6951.
- (8) Yu, Y.; Zhang, Q.; Liu, B.; Lee, J. Y. Synthesis of Nanocrystals with Variable High-Index Pd Facets through the Controlled Heteroepitaxial Growth of Trisoctahedral Au Templates. *J. Am. Chem. Soc.* **2010**, *132*, 18258–18265.
- (9) Lide, D. R. *CRC Handbook of Chemistry and Physics*, 96th ed.; CRC Press: Boca Raton, FL, 2015.
- (10) Liu, C.; Bader, S. D. Absence of Ferromagnetism in Epitaxial Films of Ultrathin Pd, Rh, and Rh on Pd Grown on Au(100). *Phys. Rev. B: Condens. Matter Mater. Phys.* **1991**, *44*, 12062–12065.
- (11) Kibler, L. A.; Kleinert, M.; Kolb, D. M. Initial Stages of Pd Deposition on Au(hkl). *Surf. Sci.* **2000**, *461*, 155–167.
- (12) Pinheiro, A. L. N.; Zei, M. S.; Luo, M. F.; Ertl, G. The Epitaxial Growth of Pd Electrodeposition on Au(100) Studied by LEED and RHEED. *Surf. Sci.* **2006**, *600*, 641–650.
- (13) Pereira, Z. S.; da Silva, E. Z. Study of Defects in Pd Thin Films on Au(100) Using Molecular Dynamics. *Phys. Rev. B: Condens. Matter Mater. Phys.* **2010**, *81*, 195417.
- (14) Naohara, H.; Ye, S.; Uosaki, K. Epitaxial Growth of a Palladium Layer on an Au(100) Electrode. *J. Electroanal. Chem.* **1999**, *473*, 2–9.
- (15) Kibler, L. A.; Kleinert, M.; Randler, R.; Kolb, D. M. Initial Stages of Pd Deposition on Au(hkl) Part I: Pd on Au(111). *Surf. Sci.* **1999**, *443*, 19–30.
- (16) Naohara, H.; Ye, S.; Uosaki, K. Electrochemical Deposition of Palladium on an Au(111) Electrode: Effects of Adsorbed Hydrogen for a Growth Mode. *Colloids Surf., A* **1999**, *154*, 201–208.
- (17) Ding, Y.; Fan, F.; Tian, Z.; Wang, Z. L. Atomic Structure of Au-Pd Bimetallic Alloyed Nanoparticles. *J. Am. Chem. Soc.* **2010**, *132*, 12480–12486.
- (18) Bhattarai, N.; Casillas, G.; Ponce, A.; Jose-Yacamán, M. Strain-Release Mechanisms in Bimetallic Core-Shell Nanoparticles as Revealed by Cs-Corrected STEM. *Surf. Sci.* **2013**, *609*, 161–166.
- (19) Liu, H. B.; Pal, U.; Perez, R.; Ascencio, J. A. Structural Transformation of Au-Pd Bimetallic Nanoclusters on Thermal Heating and Cooling: A Dynamic Analysis. *J. Phys. Chem. B* **2006**, *110*, 5191–5195.
- (20) Pryor, A.; Rana, A.; Xu, R.; Rodriguez, J. A.; Yang, Y.; Gallagher-Jones, M.; Jiang, H.; Kanhaiya, K.; Nathanson, M.; Park, J.; Kim, S.; Kim, S.; Nam, D.; Yue, Y.; Fan, J.; Sun, Z.; Zhang, B.; Gardner, D. F.; Dias, C. S. B.; Joti, Y.; et al. Single-Shot 3D Coherent Diffractive Imaging of Core-Shell Nanoparticles with Elemental Specificity. *Sci. Rep.* **2018**, *8*, 8284.
- (21) Heinz, H.; Lin, T.-J.; Mishra, R. K.; Emami, F. S. Thermodynamically Consistent Force Fields for the Assembly of Inorganic, Organic, and Biological Nanostructures: The INTERFACE Force Field. *Langmuir* **2013**, *29*, 1754–1765.
- (22) Heinz, H.; Vaia, R. A.; Farmer, B. L.; Naik, R. R. Accurate Simulation of Surfaces and Interfaces of Face-Centered Cubic Metals Using 12–6 and 9–6 Lennard-Jones Potentials. *J. Phys. Chem. C* **2008**, *112*, 17281–17290.
- (23) Xu, R.; Chen, C.-C.; Wu, L.; Scott, M.; Theis, W.; Ophus, C.; Bartels, M.; Yang, Y.; Ramezani-Dakhel, H.; Sawaya, M. R.; Heinz, H.; Marks, L. D.; Ercius, P.; Miao, J. Three-Dimensional Coordinates of Individual Atoms in Materials Revealed by Electron Tomography. *Nat. Mater.* **2015**, *14*, 1099.
- (24) Yang, Y.; Chen, C.-C.; Scott, M. C.; Ophus, C.; Xu, R.; Pryor, A.; Wu, L.; Sun, F.; Theis, W.; Zhou, J.; Eisenbach, M.; Kent, P. R. C.; Sabirianov, R. F.; Zeng, H.; Ercius, P.; Miao, J. Deciphering Chemical Order/Disorder and Material Properties at the Single-Atom Level. *Nature* **2017**, *542*, 75.

- (25) Miao, J.; Ercius, P.; Billinge, S. J. L. Atomic Electron Tomography: 3D Structures without Crystals. *Science* **2016**, *353*, aaf2157.
- (26) Shan, B.; Wang, L.; Yang, S.; Hyun, J.; Kapur, N.; Zhao, Y.; Nicholas, J. B.; Cho, K. First-Principles-Based Embedded Atom Method for PdAu Nanoparticles. *Phys. Rev. B: Condens. Matter Mater. Phys.* **2009**, *80*, 035404.
- (27) Simmons, G. *Single Crystal Elastic Constants and Calculated Aggregate Properties: A Handbook*, 2nd ed.; M.I.T. Press: Cambridge, MA, 1971.
- (28) Foiles, S. M.; Baskes, M. I.; Daw, M. S. Embedded-Atom-Method Functions for the FCC Metals Cu, Ag, Au, Ni, Pd, Pt, and Their Alloys. *Phys. Rev. B: Condens. Matter Mater. Phys.* **1986**, *33*, 7983–7991.
- (29) Singh-Miller, N. E.; Marzari, N. Surface Energies, Work Functions, and Surface Relaxations of Low-Index Metallic Surfaces from First Principles. *Phys. Rev. B: Condens. Matter Mater. Phys.* **2009**, *80*, 235407.
- (30) Tyson, W. R.; Miller, W. A. Surface Free-Energies of Solid Metals - Estimation from Liquid Surface-Tension Measurements. *Surf. Sci.* **1977**, *62*, 267–276.
- (31) Mehl, M. J.; Papaconstantopoulos, D. A. Applications of a Tight-Binding Total-Energy Method for Transition and Noble Metals: Elastic Constants, Vacancies, and Surfaces of Monatomic Metals. *Phys. Rev. B: Condens. Matter Mater. Phys.* **1996**, *54*, 4519–4530.
- (32) Elsner, B. A. M.; Müller, S.; Bargmann, S.; Weissmüller, J. Surface Excess Elasticity of Gold: Ab Initio Coefficients and Impact on the Effective Elastic Response of Nanowires. *Acta Mater.* **2017**, *124*, 468–477.
- (33) Hartford, J.; von Sydow, B.; Wahnström, G.; Lundqvist, B. I. Peierls Barriers and Stresses for Edge Dislocations in Pd and Al Calculated From First Principles. *Phys. Rev. B: Condens. Matter Mater. Phys.* **1998**, *58*, 2487–2496.
- (34) Dillamore, I. L.; Smallman, R. E.; Roberts, W. T. A Determination of the Stacking-Fault Energy of Some Pure F.C.C. Metals. *Philos. Mag.* **1964**, *9*, 517–526.
- (35) Murr, L. E. *Interfacial Phenomena in Metals and Alloys*; Addison-Wesley Publishing Company: United States, 1975.
- (36) Suzuki, H.; Barrett, C. S. Deformation Twinning in Silver-Gold Alloys. *Acta Metall.* **1958**, *6*, 156–165.
- (37) Kibey, S.; Liu, J. B.; Johnson, D. D.; Sehitoglu, H. Predicting Twinning Stress in FCC Metals: Linking Twin-Energy Pathways to Twin Nucleation. *Acta Mater.* **2007**, *55*, 6843–6851.
- (38) Miao, J.; Charalambous, P.; Kirz, J.; Sayre, D. Extending the Methodology of X-Ray Crystallography to Allow Imaging of Micrometre-Sized Non-Crystalline Specimens. *Nature* **1999**, *400*, 342.
- (39) Robinson, I.; Harder, R. Coherent X-Ray Diffraction Imaging of Strain at the Nanoscale. *Nat. Mater.* **2009**, *8*, 291.
- (40) Miao, J.; Ishikawa, T.; Robinson, I. K.; Murnane, M. M. Beyond Crystallography: Diffractive Imaging Using Coherent X-Ray Light Sources. *Science* **2015**, *348*, 530–535.
- (41) Shechtman, Y.; Eldar, Y. C.; Cohen, O.; Chapman, H. N.; Miao, J.; Segev, M. Phase Retrieval with Application to Optical Imaging: A Contemporary Overview. *IEEE Sig. Proc. Mag.* **2015**, *32*, 87–109.
- (42) Chapman, H. N.; Barty, A.; Bogan, M. J.; Boutet, S.; Frank, M.; Hau-Riege, S. P.; Marchesini, S.; Woods, B. W.; Bajt, S.; Benner, W. H.; London, R. A.; Plönjes, E.; Kuhlmann, M.; Treusch, R.; Düsterer, S.; Tschentscher, T.; Schneider, J. R.; Spiller, E.; Möller, T.; Bostedt, C.; et al. Femtosecond Diffractive Imaging with a Soft-X-Ray Free-Electron Laser. *Nat. Phys.* **2006**, *2*, 839.
- (43) Raines, K. S.; Salha, S.; Sandberg, R. L.; Jiang, H.; Rodríguez, J. A.; Fahimian, B. P.; Kapteyn, H. C.; Du, J.; Miao, J. Three-Dimensional Structure Determination from a Single View. *Nature* **2010**, *463*, 214.
- (44) Xu, R.; Jiang, H.; Song, C.; Rodríguez, J. A.; Huang, Z.; Chen, C.-C.; Nam, D.; Park, J.; Gallagher-Jones, M.; Kim, S.; Kim, S.; Suzuki, A.; Takayama, Y.; Oroguchi, T.; Takahashi, Y.; Fan, J.; Zou, Y.; Hatsui, T.; Inubushi, Y.; Kameshima, T.; et al. Single-Shot Three-Dimensional Structure Determination of Nanocrystals with Femtosecond X-Ray Free-Electron Laser Pulses. *Nat. Commun.* **2014**, *5*, 4061.
- (45) Scott, M. C.; Chen, C.-C.; Mecklenburg, M.; Zhu, C.; Xu, R.; Ercius, P.; Dahmen, U.; Regan, B. C.; Miao, J. Electron Tomography at 2.4-Ångström Resolution. *Nature* **2012**, *483*, 444.
- (46) Chen, C.-C.; Zhu, C.; White, E. R.; Chiu, C.-Y.; Scott, M. C.; Regan, B. C.; Marks, L. D.; Huang, Y.; Miao, J. Three-Dimensional Imaging of Dislocations in a Nanoparticle at Atomic Resolution. *Nature* **2013**, *496*, 74.
- (47) Zhou, J.; Yang, Y.; Yang, Y.; Kim, D. S.; Yuan, A.; Tian, X.; Ophus, C.; Sun, F.; Schmid, A. K.; Nathanson, M.; Heinz, H.; An, Q.; Zeng, H.; Ercius, P.; Miao, J. Capturing Nucleation at 4D Atomic Resolution. arXiv:1807.10709, <https://arxiv.org/abs/1807.10709>, 2018.
- (48) Plimpton, S. Fast Parallel Algorithms for Short-Range Molecular Dynamics. *J. Comput. Phys.* **1995**, *117*, 1–19.
- (49) Stukowski, A. Visualization and Analysis of Atomistic Simulation Data with OVITO—the Open Visualization Tool. *Modell. Simul. Mater. Sci. Eng.* **2010**, *18*, 015012.
- (50) Heinz, H.; Ramezani-Dakhel, H. Simulations of Inorganic-Bioorganic Interfaces to Discover New Materials: Insights, Comparisons to Experiment, Challenges, and Opportunities. *Chem. Soc. Rev.* **2016**, *45*, 412–448.
- (51) Ramezani-Dakhel, H.; Ruan, L. Y.; Huang, Y.; Heinz, H. Molecular Mechanism of Specific Recognition of Cubic Pt Nanocrystals by Peptides and the Concentration-Dependent Formation from Seed Crystals. *Adv. Funct. Mater.* **2015**, *25*, 1374–1384.
- (52) Gupta, A.; Boekfa, B.; Sakurai, H.; Ehara, M.; Priyakumar, U. D. Structure, Interaction, and Dynamics of Au/Pd Bimetallic Nanoalloys Dispersed in Aqueous Ethylpyrrolidone, a Monomeric Moiety of Polyvinylpyrrolidone. *J. Phys. Chem. C* **2016**, *120*, 17454–17464.
- (53) Geada, I. L.; Ramezani-Dakhel, H.; Jamil, T.; Sulpizi, M.; Heinz, H. Insight into Induced Charges at Metal Surfaces and Biointerfaces Using a Polarizable Lennard–Jones Potential. *Nat. Commun.* **2018**, *9*, 716.
- (54) Ramezani-Dakhel, H.; Mirau, P. A.; Naik, R. R.; Knecht, M. R.; Heinz, H. Stability, Surface Features, and Atom Leaching of Palladium Nanoparticles: Toward Prediction of Catalytic Functionality. *Phys. Chem. Chem. Phys.* **2013**, *15*, 5488–5492.
- (55) Ruan, L.; Ramezani-Dakhel, H.; Lee, C.; Li, Y.; Duan, X.; Heinz, H.; Huang, Y. A Rational Biomimetic Approach to Structure Defect Generation in Colloidal Nanocrystals. *ACS Nano* **2014**, *8*, 6934–6944.
- (56) Ramezani-Dakhel, H.; Bedford, N. M.; Woehl, T. J.; Knecht, M. R.; Naik, R. R.; Heinz, H. Nature of Peptide Wrapping onto Metal Nanoparticle Catalysts and Driving Forces for Size Control. *Nanoscale* **2017**, *9*, 8401–8409.
- (57) Liu, J.; Tennessen, E.; Miao, J.; Huang, Y.; Rondinelli, J. M.; Heinz, H. Understanding Chemical Bonding in Alloys and the Representation in Atomistic Simulations. *J. Phys. Chem. C* **2018**, *122*, 14996–15009.
- (58) Rosengaard, N. M.; Skriver, H. L. Calculated Stacking-Fault Energies of Elemental Metals. *Phys. Rev. B: Condens. Matter Mater. Phys.* **1993**, *47*, 12865–12873.
- (59) Cai, J.; Wang, F.; Lu, C.; Wang, Y. Y. Structure and Stacking-Fault Energy in Metals Al, Pd, Pt, Ir, and Rh. *Phys. Rev. B: Condens. Matter Mater. Phys.* **2004**, *69*, 224104.